Supplement of Atmos. Chem. Phys., 23, 10697–10711, 2023
https://doi.org/10.5194/acp-23-10697-2023-supplement

Supplement of

Enrichment of calcium in sea spray aerosol: insights from bulk measurements and individual particle analysis during the R/V *Xuelong* cruise in the summertime in Ross Sea, Antarctica

Bojiang Su et al.

Correspondence to: Lei Li (lileishdx@163.com) and Guohua Zhang (zhanggh@gig.ac.cn)

Table of contents

Note: Figures S11-S20 were used when discussing supplementary Text (S3-S5) and were not cited in the main text.

Introduction: This supplement contains additional information on the comparative analysis.

Text S1. Uncertainty analysis and quality assurance of datasets

IGAC: The water-soluble ion mass concentrations were analyzed by using an ion chromatography (IC) system (Dionex ICS-3000) within an in-situ Gas and Aerosol Compositions monitoring system (IGAC, Model S-611). Before the sampling, a known concentration of LiBr was used as an internal standard by adding to the aerosol liquid samples to determine the stability of the IGAC system. The changes in the internal standard were within 5%. Subsequently, the IC was calibrated by using six to eight concentrations of stand solutions (0.1-2000 μg L^{-1}), depending on the target species and concentrations, in which the R^2 was above 0.99. The calibration curves for each ion could be found in our previous studies (Yan et al., 2019; Yan et al., 2020a; Yan et al., 2020b). The uncertainty of the IC systems was generally less than 5% for all analyzed ionic species. The detection limits for Na^+, Cl^-, Ca^{2+}, K^+, and Mg^{2+} were 0.03, 0.03, 0.019, 0.011, and 0.042 μg L^{-1} (aqueous solution), respectively. During the whole sampling period (hourly temporal resolution), the detection rate for Na^+, Cl^-, Ca^{2+}, K^+, and Mg^{2+} were 98.5% (1178 of 1196), 92.6% (1108 of 1196), 88.2% (1055 of 1196), 98.9% (1183 of 1196), and 98.5% (1178 of 1196), respectively. All values below the detection limit were omitted before analysis. The undetected rate for both Ca^{2+} and Na^+ was approximately 12%. **Figure S11** shows the time series of observed ion mass concentrations and EF_{Ca}. The ion mass concentrations were above the detection limit. Particularly, the mean Na^+ and Ca^{2+} mass concentrations were 364.64 ng m^{-3} (ranging from 6.66 to 4580.10 ng m^{-3}) and 21.20 ng m^{-3} (ranging from 0.27 to 334.40 ng m^{-3}), respectively, which were far above (> 10 times) the detection limit. Such data indicate that the variations of EF_{Ca} would not suffer the increasing uncertainties when the ion mass concentrations near the detection limit. Thus, we suggest that the data on ion mass concentration is reliable and representative.

Given that the measured mass concentrations of Ca^{2+} and Na^+ were far above the detection limit, we only considered the systematic errors (< 5%) of the mass concentrations of Ca^{2+} and Na^+. Based on the variations of extreme value, the uncertainty of each EF_{Ca} is calculated as below:

$$abs\left(1-\frac{\frac{0.95*Ca^{2+}_{conc.}}{1.05*Na^{+}_{conc.}}/0.038}{\frac{Ca^{2+}_{conc.}}{Na^{+}_{conc.}}/0.038}\right)\approx 9.5\% < Unc_{(EFCa)} < abs\left(1-\frac{\frac{1.05*Ca^{2+}_{conc.}}{0.95*Na^{+}_{conc.}}/0.038}{\frac{Ca^{2+}_{conc.}}{Na^{+}_{conc.}}/0.038}\right)\approx 10.5\%$$

Where $Ca^{2+}_{conc.}$ and $Na^{+}_{conc.}$ represent the observed ion mass concentration of Ca^{2+} and Na^+, respectively. 0.038 is the ratio of Ca^{2+} to Na^+ in seawater. 0.95 and 1.05 represent the variations of extreme value. The largest uncertainty of EF_{Ca} ($Unc_{(EFCa)}$) would be estimated lower than 11%.

SPAMS: Even though SPAMS has advantages for investigating the chemical characteristics and evolutionary mechanisms of individual particles, it is still quite challenging for it to provide quantitative evidence, as it is limited by the potential matrix effects, laser inhomogeneities, and transmission efficiencies of the aerodynamic lenses (Qin et al., 2006; Pratt and Prather, 2012). Nevertheless, the results via SPAMS are also reliable because of its broad datasets with high temporal resolution. Therefore, the analyses of particle count, size, and chemical composition (by peak area) can be considered semi-quantitative from a statistical perspective (Healy et al., 2012; Su et al., 2021a; Zhang et al., 2021).

Text S2. Single-particle characteristics of other observed particles

In this study, a total of ~ 930, 000 particles with mass spectral information and D_{va} were measured using SPAMS and manually clustered into the seven single-particle groups of SS (sea salt aerosol), SS-aged (aged sea salt aerosol), SS-Bio (sea salt with biogenic organic matter), OC-Ca (internally mixed organics with calcium), OC-K (internally mixed organics with potassium), OC (organic-carbon-dominated), and EC (element carbon) (**Table S2**). Based on their different mass spectral characteristics (Prather et al., 2013; Collins et al., 2014; Guasco et al., 2014; Su et al., 2021b), we briefly describe all of them (except for OC-Ca) as follows (**Figure S5**):

SS is identified by prominent ion markers that are associated with Na and Cl (e.g., *m/z* 23 $[Na]^+$, 46 $[Na_2]^+$, 81 $[Na_2{}^{35}Cl]^+$, 83 $[Na_2{}^{37}Cl]^+$, -35 $[^{35}Cl]^-$, and -37 $[^{37}Cl]^-$), and smaller contributions of other inorganic matter that are known to exist in seawater (i.e., Mg, K, Ca). SS accounted for 16.5% of the particles obtained during the observation cruise, with a peak of ~ 1. μm in D_{va}.

SS-aged can be regarded as SS with atmospheric aging, with additional characteristic peaks of nitrate (*m/z* -46 $[NO_2]^-$ and -62 $[NO_3]^-$). SS-aged presented a similar size distribution as SS, with a proportion of 8.1%.

SS-Bio is characterized by a large ratio of organic ion signatures of organic nitrogen (*m/z* -26 $[CN]^-$ and -42 $[CNO]^-$), phosphate (*m/z* -63 $[PO_2]^-$ and -79 $[PO_3]^-$), carbohydrate (*m/z* -45 $[CHO_2]^-$, -59 $[C_2H_3O_2]^-$, and -73 $[C_3H_5O_2]^-$), siliceous materials (*m/z* -60 $[SiO_2]^-$), and organic carbon (*m/z* 27 $[C_2H_3]^+$ and 43 $[C_2H_3O_3]^+$), in addition to the aforementioned inorganic salt-related ion signature (e.g., 23 $[Na]^+$). SS-Bio accounted for only 3.1% of the particles obtained during the observation cruise, with a peak of ~ 0.9 μm in D_{va}.

OC-K is identified by the dominant presence of K (*m/z* 39) and the aforementioned organic species and exhibited the third largest proportion (13.7%). OC-K was scattered in the D_{va} range of 0.2 to 1.0 μm, peaking at 0.6 μm. Similar to OC-Ca, this chemical class may also be associated with biogenic origin, which may originate from intact heterotrophic bacterial cells, fragments of cells, and bacterial exudates (Gaston et al., 2011; Guasco et al., 2014; Sierau et al., 2014).

OC exhibits a significant proportion of organic signals of organic carbon and organic nitrogen. This single-particle type may originate from not only heterogeneous nucleation with the oxidation of monoterpene and isoprene but also anthropogenic emissions (e.g., ship emissions). However, we suggest that it is more likely to be related to the biogenic origin of the bacteria and phytoplankton.

Text S3. A comparative analysis of the chemical composition, particle size, counts, and mixing state via SPAMS between leg I and leg II

Based on the SPAMS datasets, we found that there was a minimal change in chemical composition (**Figs. S12** and **S13**), particle size (**Fig. S14**) and counts (**Fig. S15**), and mixing state (**Figs. S16** and **S17**) of the obtained particles (especially SS-Bio, OC-Ca, and OC-K) during leg I (sea ice period) and leg II (period without Sea ice). This suggests that the existence of sea ice may play an insignificant role in the intrinsic physicochemical properties of the obtained particles ranging from 0.2 to 2 μm.

Text S4. Potassium (K^+) and magnesium (Mg^{2+}) enrichment in sea spray aerosols induced by temperature, wind speed, and sea ice

The enrichment factors of K^+ (EF_K) and Mg^{2+} (EF_{Mg}) were calculated by using the same equation described in the main text. Generally, the ratios of K^+ and Mg^{2+} to Na^+ in seawater are 0.0218 and 0.1112, respectively (Hara et al., 2012; Boreddy and Kawamura, 2015; Su et al., 2022).

During the observation cruise, EF_K (ranging from 0.20 to 75, with a median and mean of 1.19 and 3.61, respectively, n > 1000) and EF_{Mg} (ranging from 0.12 to 26.94, with a median and mean of 1.48 and 2.46, respectively, n > 1000) were also observed.

Figure S18 shows the enrichment factors of K^+ and Mg^{2+} with respect to sodium in bulk aerosols at different ambient temperatures (≥ -3.5°C and < -3.5°C), wind speeds (≥ 7 m s^{-1} and < 7 m s^{-1}), and sea ice fraction (with and without sea ice) during the whole sampling period. The results were very similar to that of calcium (Ca^{2+}) enrichment in sea spray aerosols (SSAs), which may present an analogous enrichment mechanism by environmental factors (e.g., ambient temperature and wind speed with sea ice) (**Fig. S19**).

We also inferred that the K^+ and Mg^{2+} enrichments in SSAs were also attributed to organically internally mixed aerosols (e.g., OC-K and SS-Bio). We propose three possible explanations for this: (i) If the released K^+ and Mg^{2+} are in the form of inorganic salts (e.g., KCl and $MgCl_2$) within SSAs, they are likely to be associated with sea salt fractionation by precipitations of sylvite ca. -33°C and 10 $H_2O{\cdot}MgCl_2$ ca. -36°C on the sea ice (Hara et al., 2012). However, the average and minimum ambient temperatures during leg I were only -4.1 °C and ~ -8 °C, respectively. Thus, sea salt fractionation on sea ice is less likely. (ii) We observed a single-particle type of OC-K with abundant K^+ (*m/z* 39) and organic ion signatures by using SPAMS during the cruise observations. Other single-particle types involving K^+ (*m/z* 39) and Mg^{2+} (*m/z* 24) also exhibited some characteristic organic peaks (e.g., in SS-Bio). (iii) K^+ and Mg^{2+} are also greatly capable of stabilizing organic supramolecular structures in the form of organic ligands (i.e., marine microgels) (Gaston et al., 2011; Cochran et al., 2016; Mukherjee et al., 2020). Based on the above discussion, we, therefore, suggest that internally mixed potassium and magnesium organics contribute to corresponding enrichment in SSAs. Analogous to OC-Ca, we also suggest that the marine microgels assembled by K^+ and Mg^{2+} to exopolymer substances (EPSs) may be emitted to the atmosphere by low wind-blown sea ice.

Text S5. Multiple linear and random forest regression

Multiple linear and random forest analyses were applied to describe the relative contribution of possible factors to the variations in EF_{Ca}. In multiple linear models, two of the most common measures of model fit are the residual standard error and proportion of variance explained (R^2), by using least squares fit. In contrast, random forest with nonlinear multiple regression has been widely applied to predict and reproduce the importance of factors, by building multiple decision trees (Lundberg et al., 2020; Zhang et al., 2021; Song et al., 2022).

We attempted to estimate the relative importance of the impact factors on EF_{Ca}, including the environmental factors (ambient temperature, wind speed, and chlorophyll-a concentration), particle types (SS-Ca and OC-Ca, by count), and relative fraction of organics in the OC-Ca particles. Multiple linear regression and random forest analysis were applied. As shown in **Fig. S20**, EF_{Ca} could not be well predicted by those possible factors for the sea ice period ($r^2 = 0.19$, $p < 0.01$) and whole sampling period ($r^2 = 0.15$, $p < 0.01$), which may be ascribed to other unknown mechanisms and/or OC-Ca with low water solubility. Future studies are needed to explore the mechanisms of calcium enrichment in SSAs.

2. Supplementary Figures

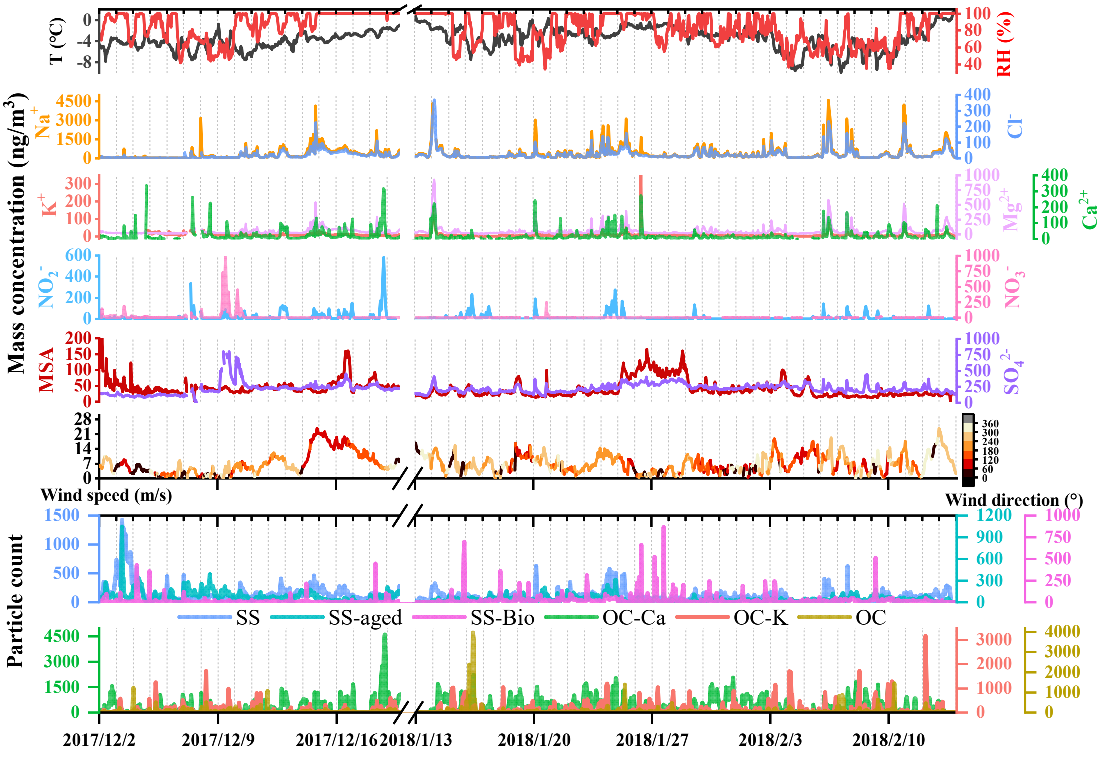

Figure S1

Time series (hourly temporal resolution) of meteorological parameters, typical water-soluble ion mass concentrations, and single-particle counts of individual particle types.

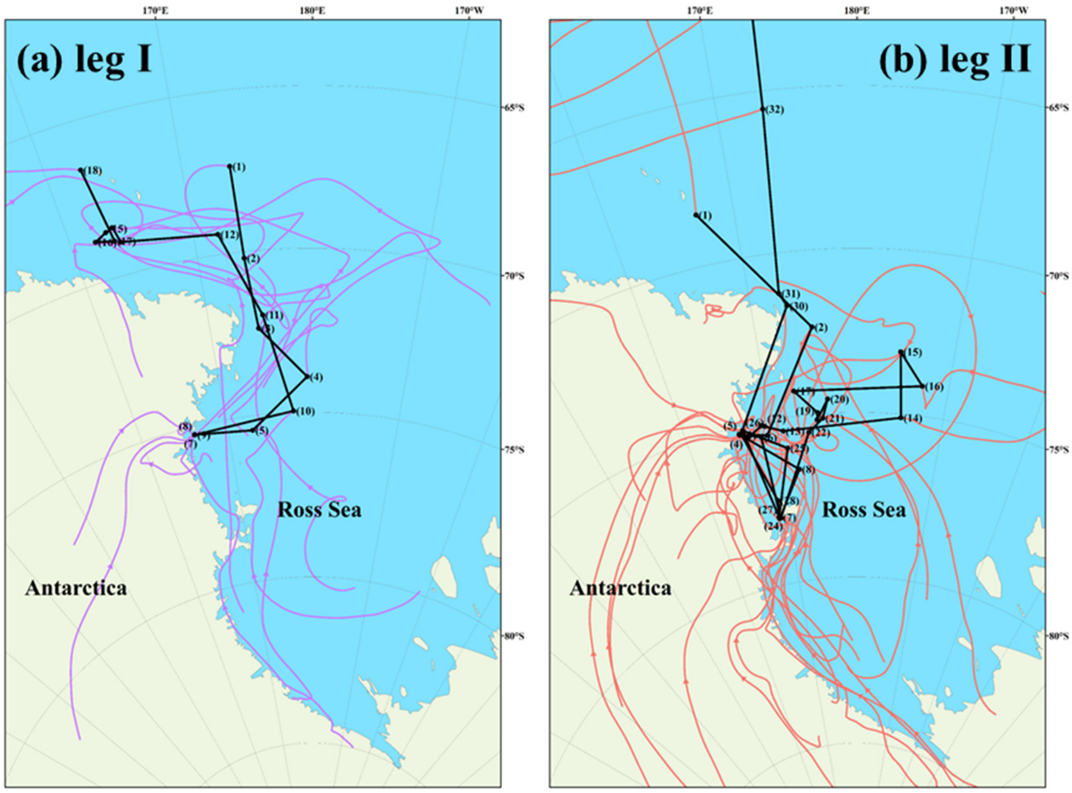

Figure S2

HYSPLIT back trajectories (72-hour) arrived at the ship location (50 m above sea level) every day (0:00 local time) during leg I (purple solid line) and leg II (red solid line). The black solid lines indicated the cruise track of the R/V *Xuelong*. The marked numbers indicated the ship location at the local time of 0:00 during the whole observation. For example, “(1)” in the leg I referred to the ship location at 0:00, on 2 December 2017, and so on.

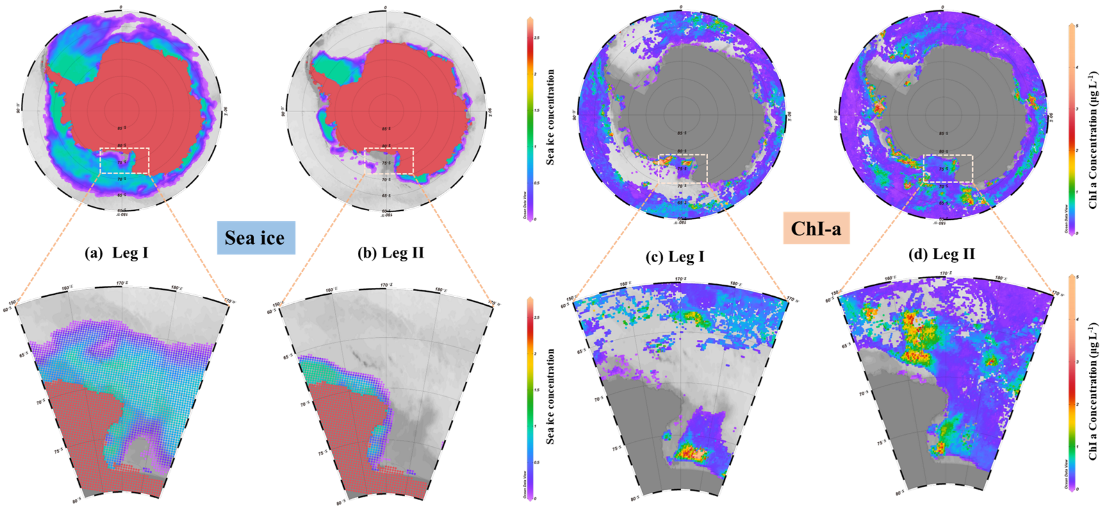

Figure S3

Average sea ice fraction and chlorophyll-a concentration during leg I (a and c) and leg II (b and d) from a satellite. This figure was created by using Ocean Data View (Schlitzer, 2002).

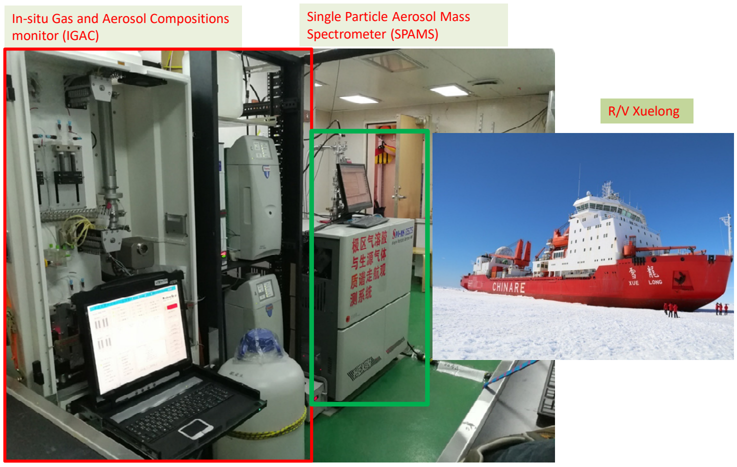

Figure S4

An in-situ Gas and Aerosol Composition monitoring system (IGAC) was used to determine the gaseous and aerosol water-soluble ion mass concentrations (red frame, left). A Single Particle Aerosol Mass Spectrometer (SPAMS) was used to measure the chemical compositions, mixing states, and particle size of individual particles (green frame, right).

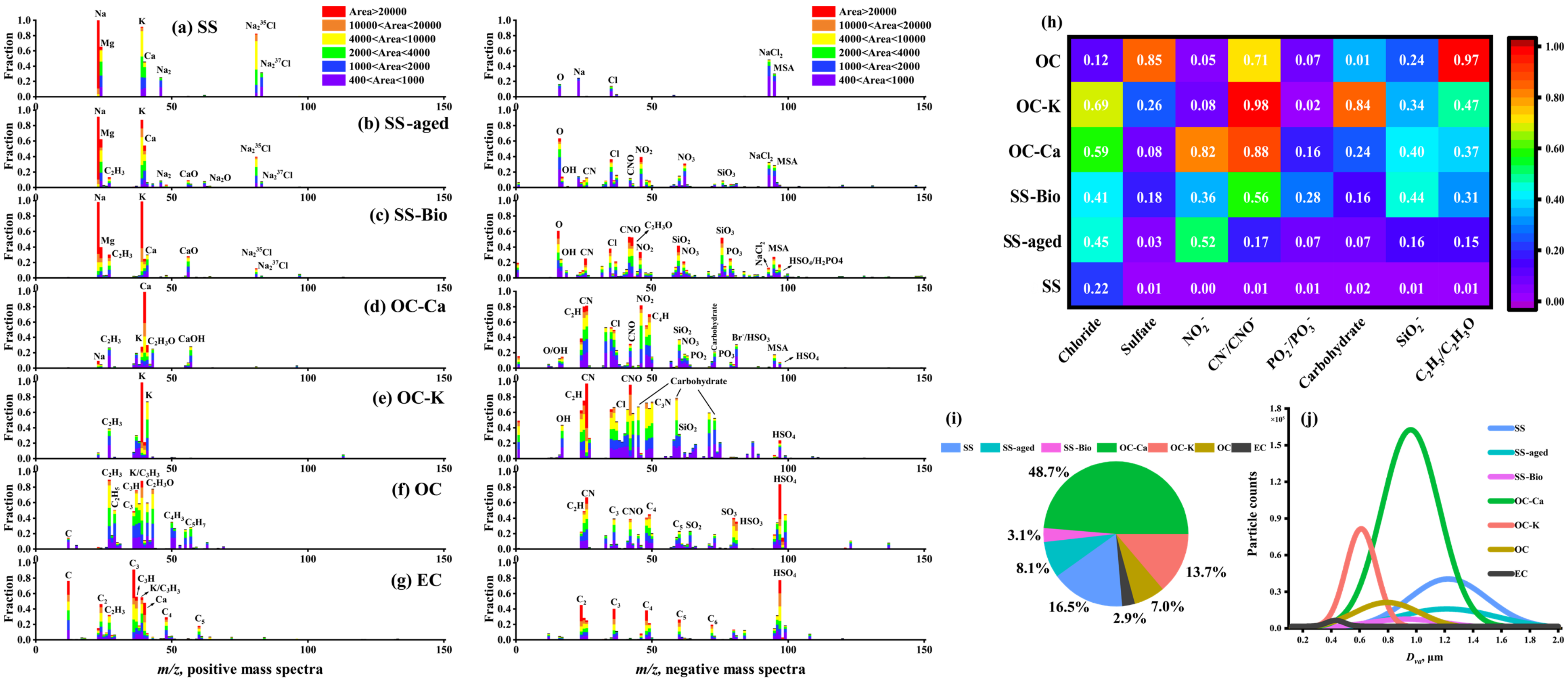

Figure S5

(a) – (g) Average digitalized single-particle mass spectra for seven classes of collected particles. (h) Hot plot of number fractions for major species of obtained single-particle types, including chloride (*m/z* -35 and -37), sulfate (*m/z* -97), nitro-containing organic species (*m/z* -46), organic nitrogen (*m/z* -26 or -42), phosphate (*m/z* -63 or -79), carbohydrate (*m/z* -45, -59, or -73), siliceous materials (*m/z* -60), and organic carbon (*m/z* 27 or 43). (i) Relative proportion of different single-particle types during the cruise observations. (j) Unscaled size-resolved number distributions of all individual particles.

A total of ~ 580, 000 calcium-containing particles (*m/z* 40 $[Ca]^+$) were observed during cruise observations, accounting for ~ 62% of the total obtained particles. These calcium-containing particles were scattered among all the obtained particle types, with proportions of ~48%, ~56%, ~25%, ~22%, ~100%, ~12%, and ~49% for SS, SS-aged, SS-Bio, OC-K, OC-Ca, OC, and EC, respectively. In particular, the SS-Ca and OC-Ca particle types accounted for ~ 12% and ~ 72% of the total calcium-containing particles and ~ 7% and ~ 50% of the total obtained particles, respectively.

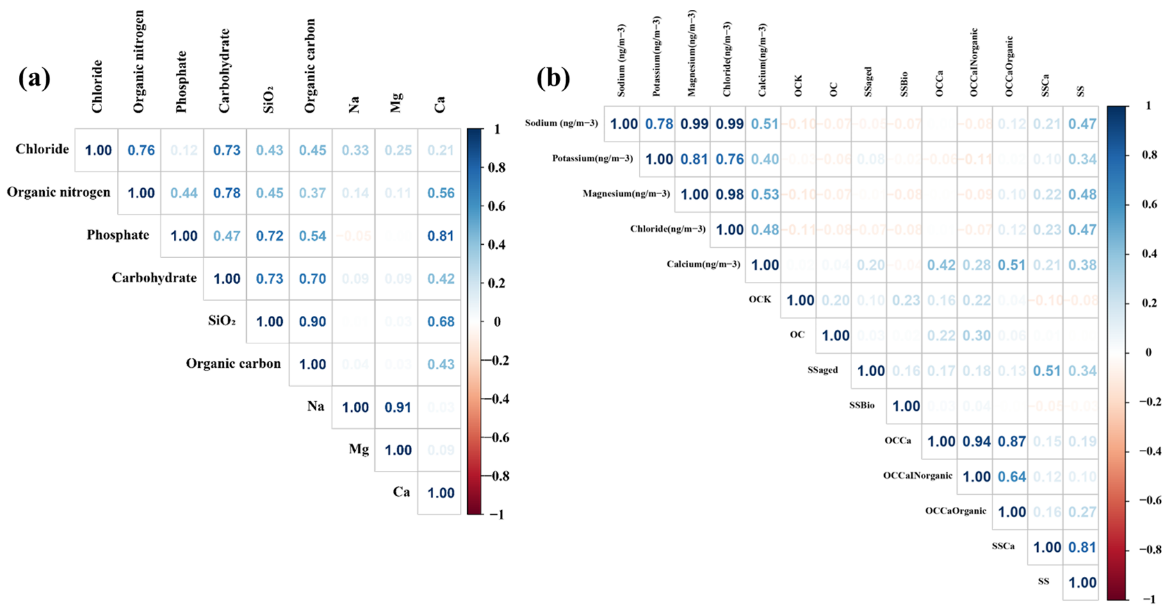

Figure S6

(a) Correlation analysis between the single-particle peak area for species in OC-Ca. There were relatively high correlation coefficients (r = 0.42–0.81) between the peak area of Ca and organic species (organic nitrogen, phosphate, carbohydrate, siliceous materials, and organic carbon). (b) Correlation analysis between the OC-Ca (by count) and mass concentration of Ca^{2+}. The first (sodium) to the fifth (chloride) referred to mass concentration. The sixth (OCK) to the fourteenth (SS) referred to single-particle types.

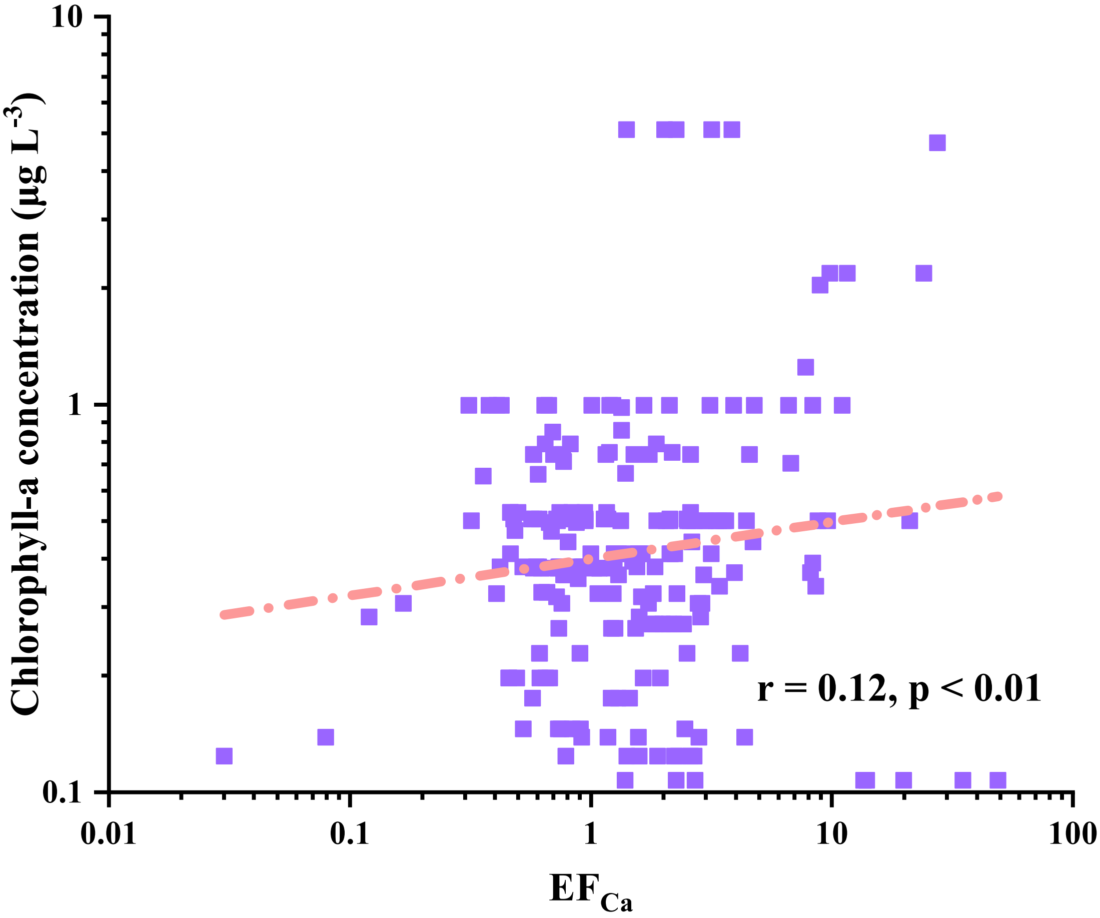

Figure S7

Correlation analysis between EF_{Ca} and chlorophyll-a concentration during leg II.

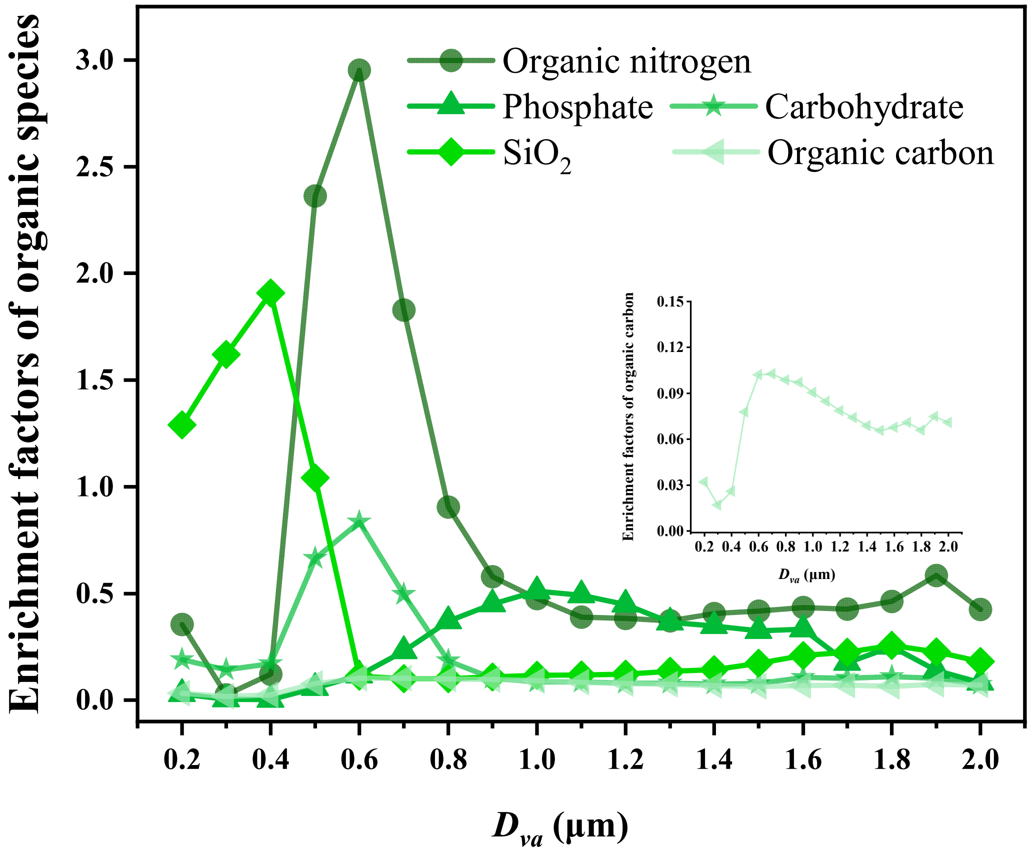

Figure S8

Size-dependent single-particle peak area ratio of organic matter to calcium. Based on SPAMS, we defined the organic matter enrichment factors as the single-particle peak area ratio of organic species to Ca (*m/z* 40) in OC-Ca. The single-particle counts of OC-Ca were 420, 000. The organic species included organic nitrogen (*m/z* -26 and -42), phosphate (*m/z* -63 and -79), carbohydrate (*m/z* -45, -59, and -73), siliceous materials (SiO_2, *m/z* -60), and organic carbon (*m/z* 27 and 43).

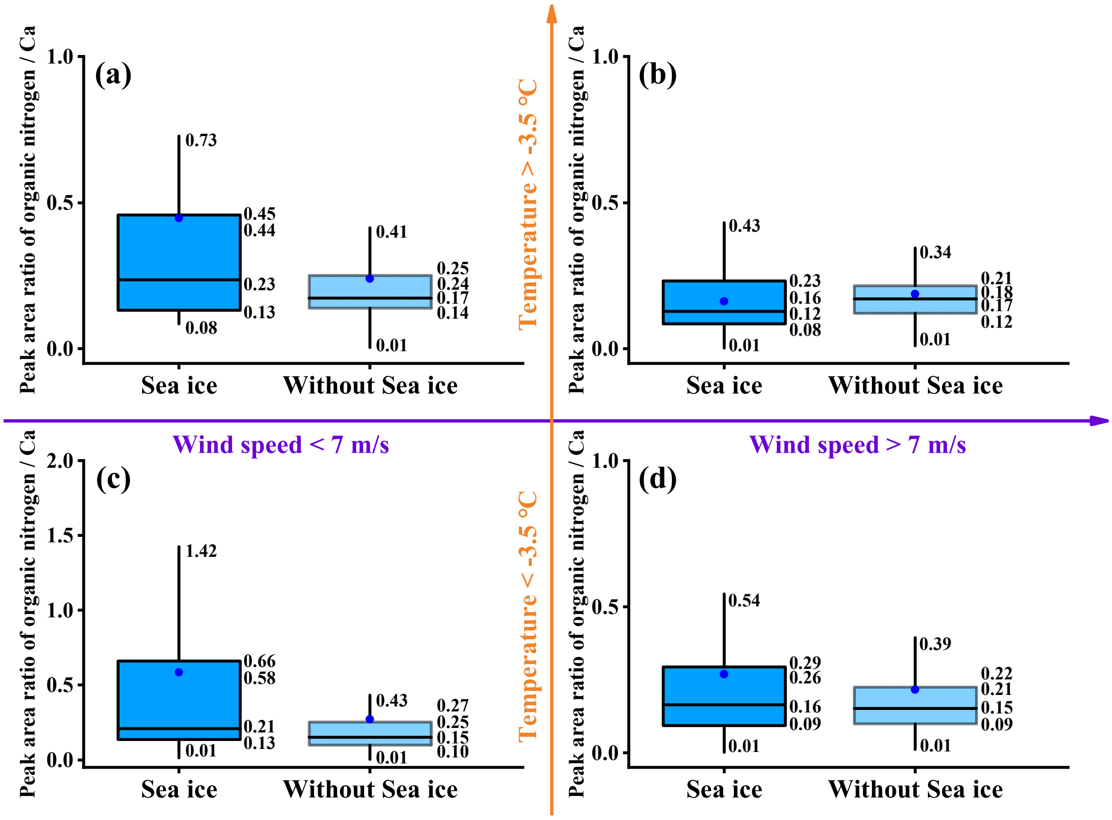

Organic nitrogen

Figure S9

A box and whisker plot of the peak area ratio of organic nitrogen (*m/z* -26 and -42) to Ca (*m/z* 40) in OC-Ca at different ambient temperatures, wind speeds, and sea ice fraction. As described above, the organic nitrogen enrichment factor in OC-Ca (EF_{ON}) is defined as the single-particle peak area ratio of organic nitrogen to calcium. We choose the organic nitrogen within OC-Ca for comparative analysis because of its large number fraction (0.88). In the box and whisker plot, the marked values from top to bottom were 90th and 75th percentiles, mean, median, and 25th and 10th percentiles, respectively.

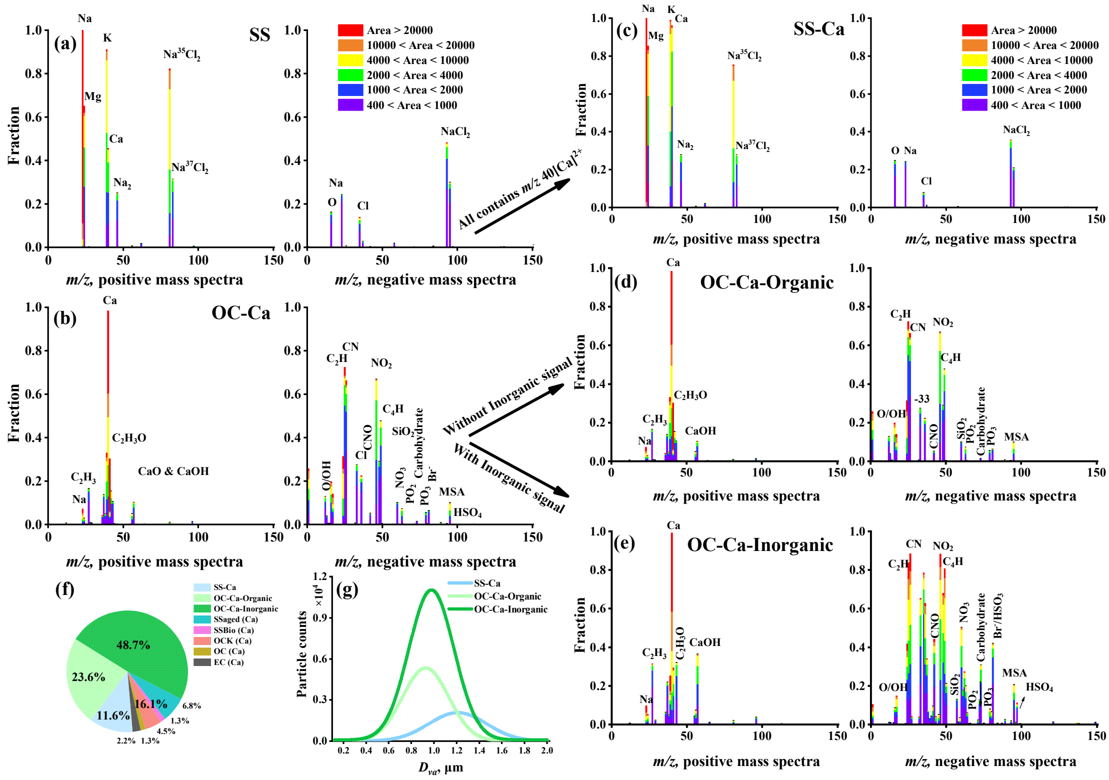

Figure S10

(a) and (b) Average digitalized single-particle mass spectra of chemical classes of SS and OC-Ca. (c) Average digitalized single-particle mass spectra of SS-Ca that are refined by using *m/z* 40 $[Ca]^{2+}$ upon SS. (d) and (e) Average digitalized single-particle mass spectra of OC-Ca-Organic and OC-Ca-Inorganic, which are classified by whether inorganic compounds (chloride (*m/z* -35 and -37), nitrate (*m/z* -62), and sulfate (*m/z* -97) ion signals are present. (f) Relative proportion and (g) unscaled size-resolved number distributions of single-particle types.

Note: Figures S11-S20 were used when discussing supplementary Text and were not cited in the main text.

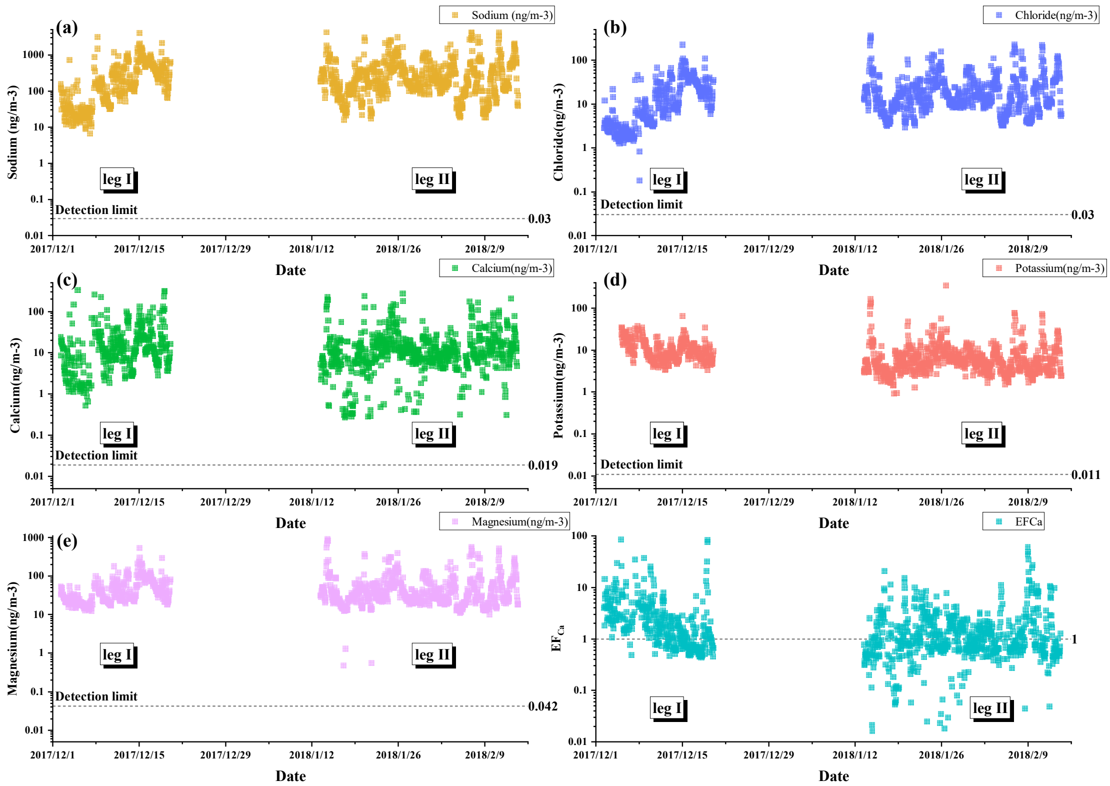

Figure S11

The time series of observed ion mass concentrations and EF_{Ca}.

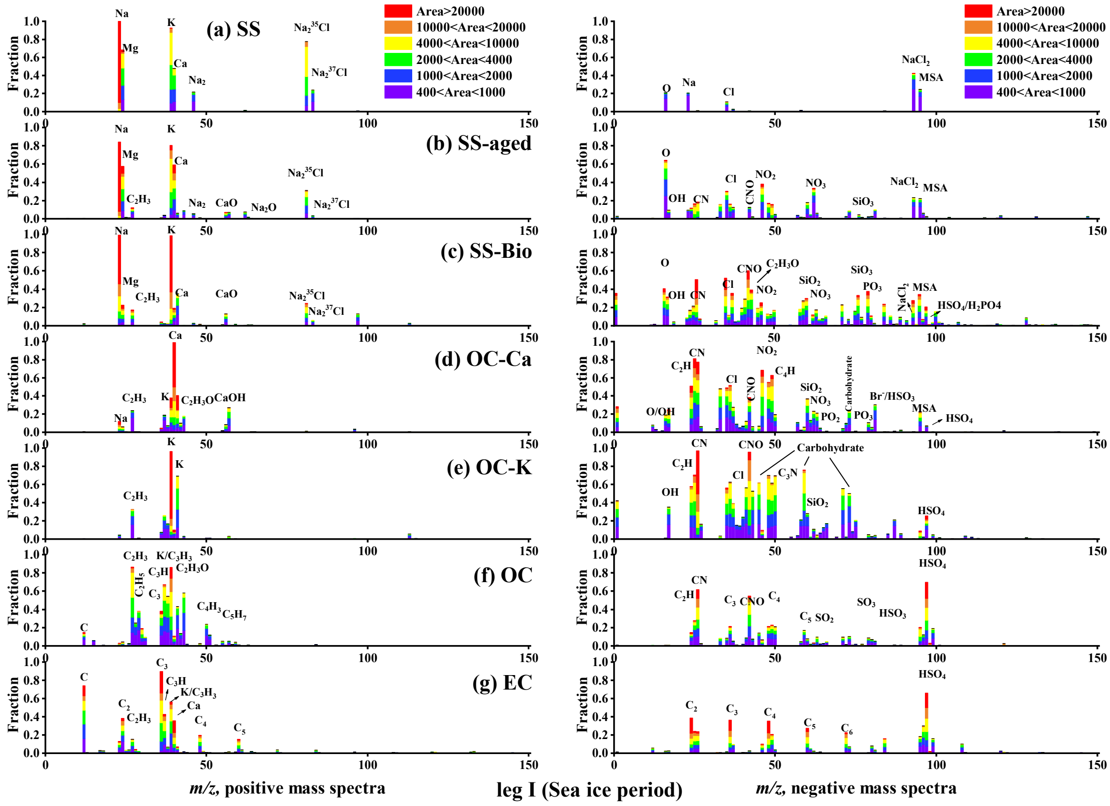

Figure S12

Average digitalized single-particle mass spectra for seven classes of collected particles during leg I (sea ice period).

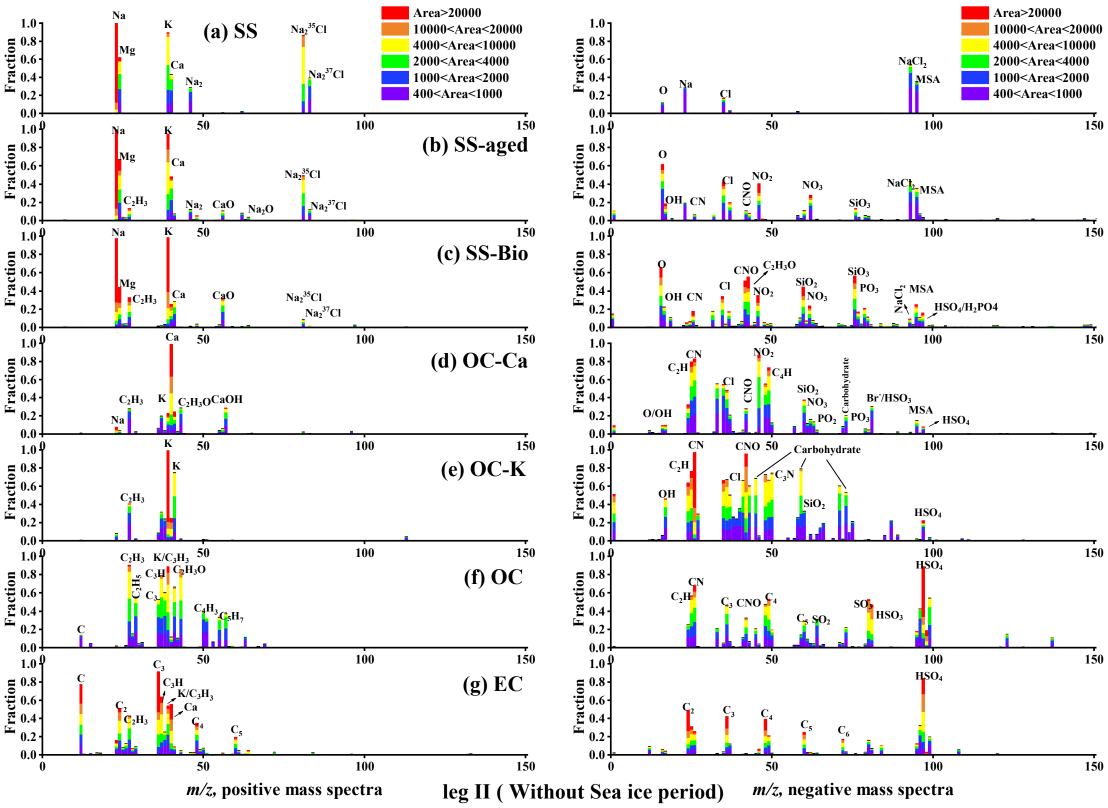

Figure S13

Average digitalized single-particle mass spectra for seven classes of collected particles during leg II (period without sea ice).

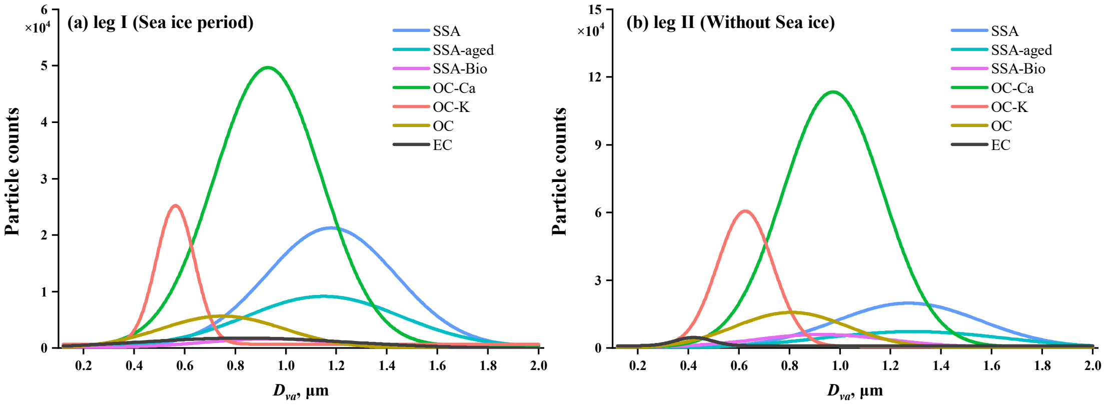

Figure S14

Unscaled size-resolved number distributions of all individual particles during leg I (sea ice period) and leg II (period without sea ice).

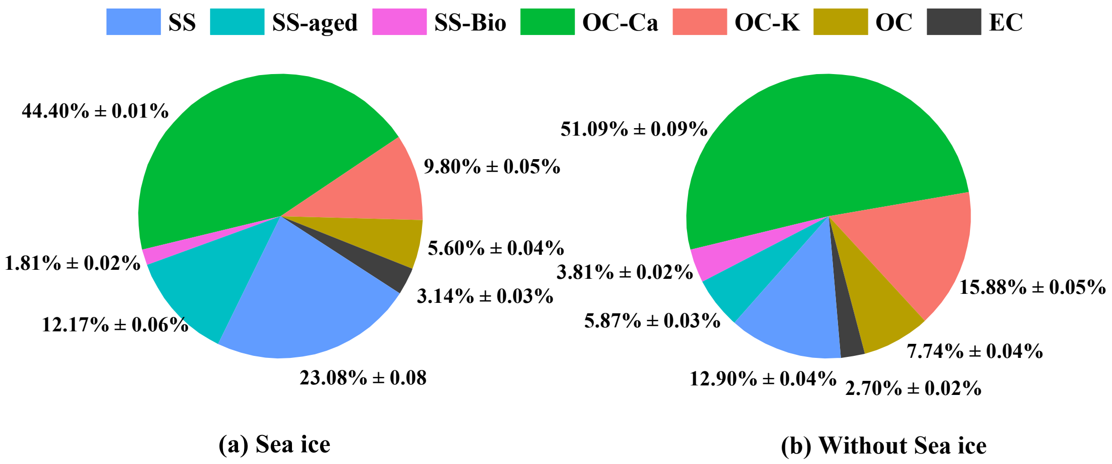

Figure S15

The relative proportion of different single-particle types during leg I (sea ice period) and leg II (period without sea ice). It is still quite a challenge to obtain quantitative measurements using SPAMS due to the potential inhomogeneities in the transmission efficiencies of the aerodynamic lenses and desorption/ionization, and the matrix effects of individual particles (Gross et al., 2000; Qin et al., 2006; Pratt and Prather, 2012). Therefore, it may not be straightforward to use the particle count in comparison with the absolute mass concentration. We noted that there was little difference in OC-Ca proportion during the periods of sea ice and without sea ice. The source of OC-Ca for the two periods may be explained by the low wind-blown sea ice and the land-based ice from Antarctica (**Fig. S2** and **Table S1**, the influence of air masses from Antarctic land, 40%), respectively. Another reason for that may be the resuspension of OC-Ca. Also, the bubble bursts within open water and leads occurred in both periods.

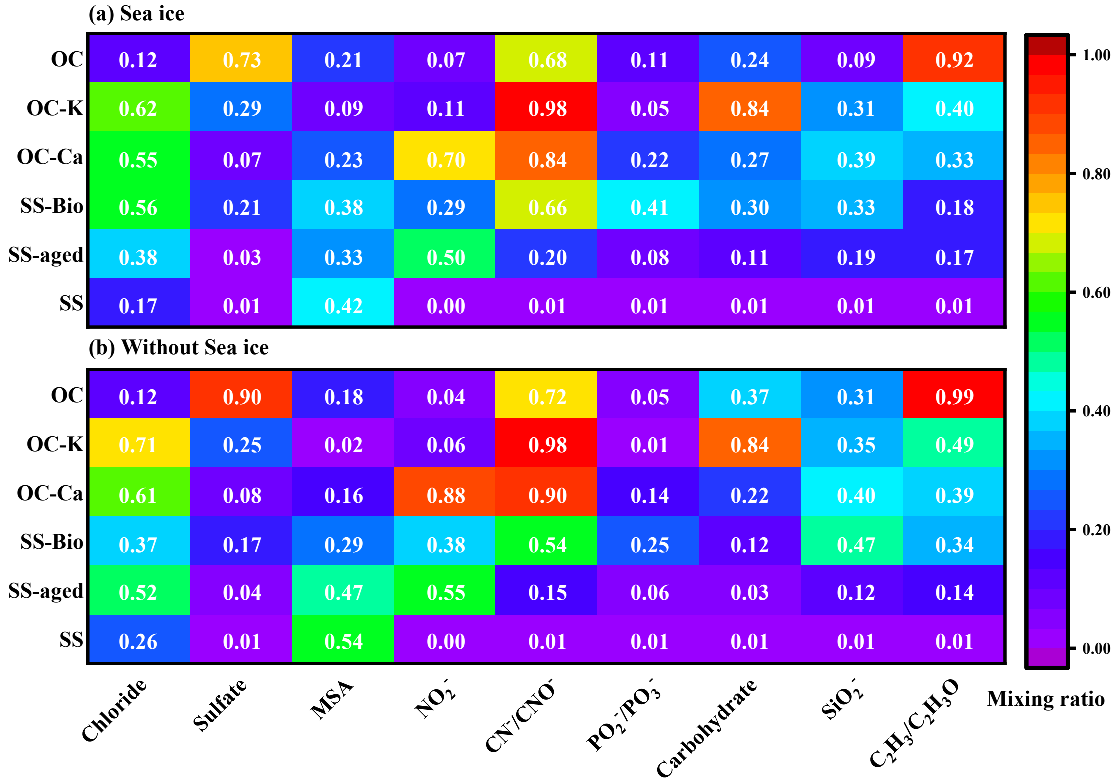

Figure S16

The hot plot of number fractions for major species of obtained single-particle types, including chloride (*m/z* -35 and -37), sulfate (*m/z* -97), methanesulfonic acid (MSA, *m/z* -95), nitro-containing organic species (*m/z* -46), organic nitrogen (*m/z* -26 or -42), phosphate (*m/z* -63 or -79), carbohydrate (*m/z* -45, -59, or -73), siliceous materials (*m/z* -60), and organic carbon (*m/z* -27 or 43). (a) leg I (sea ice period) and leg II (period without sea ice).

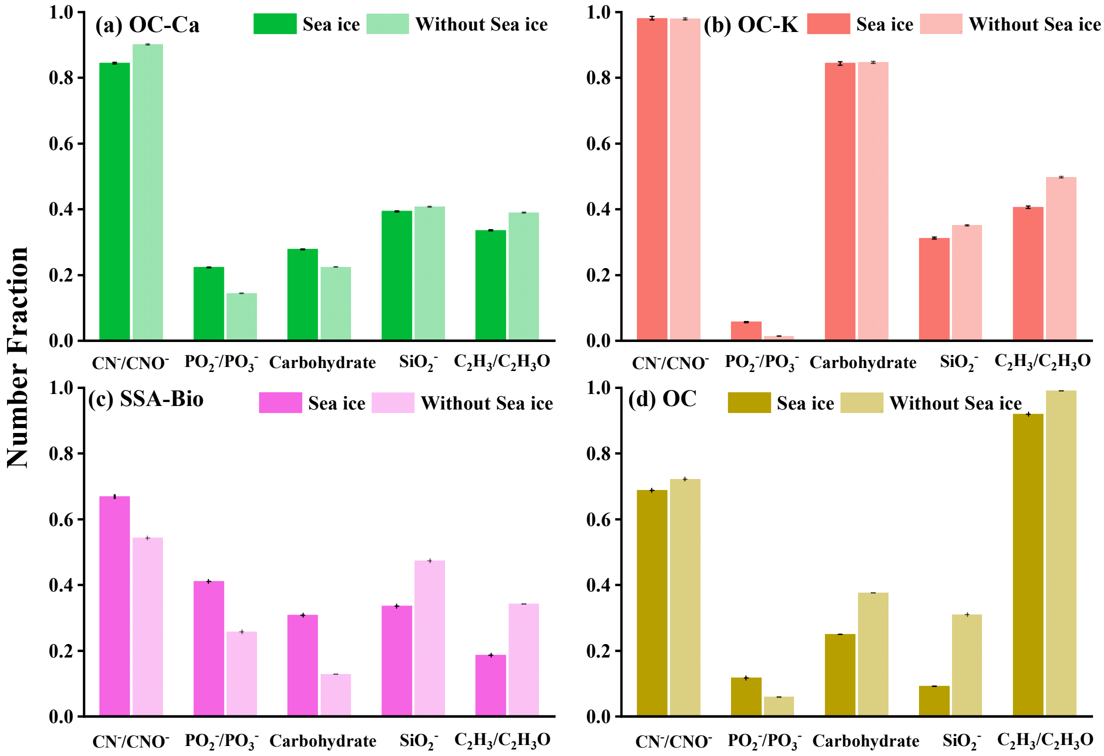

Figure S17

Comparison by number fractions for some typical organic chemical components of (a) OC-Ca, (b) OC-K, and (c) SS-Bio during leg I (sea ice period) and leg II (period without Sea ice). The errors are calculated assuming Poisson statistics for the obtained particles.

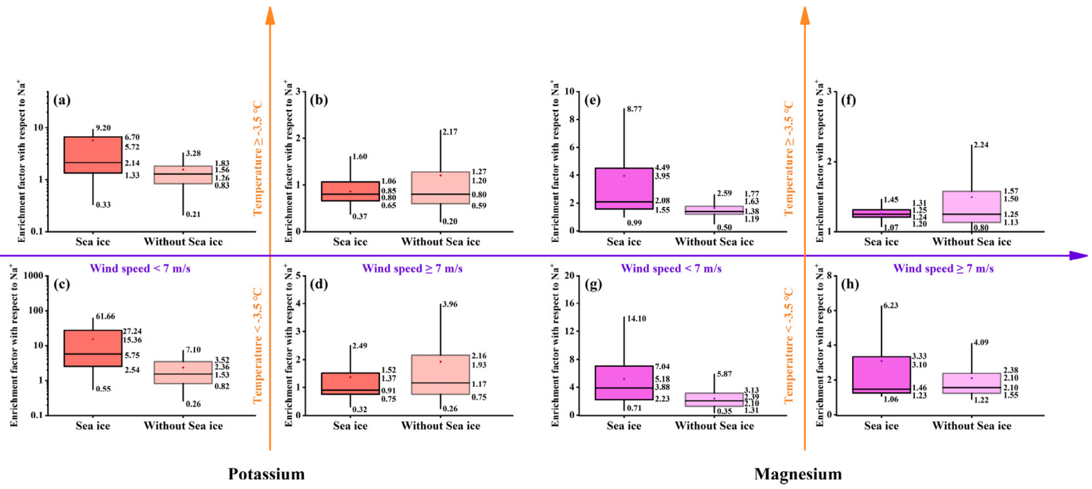

Figure S18

Box and whisker plots of hourly Ca^{2+} enrichment factor (EF_{Ca}) with respect to Na^{+} at different ambient temperatures, wind speeds, and sea ice fraction. In the box and whisker plots, the marked values from top to bottom are the 90th and 75th percentiles, mean, median, and 25th and 10th percentiles, respectively. In comparison with the bubble charts (Fig. S15), the box and whisker plot present similar intentions with different forms.

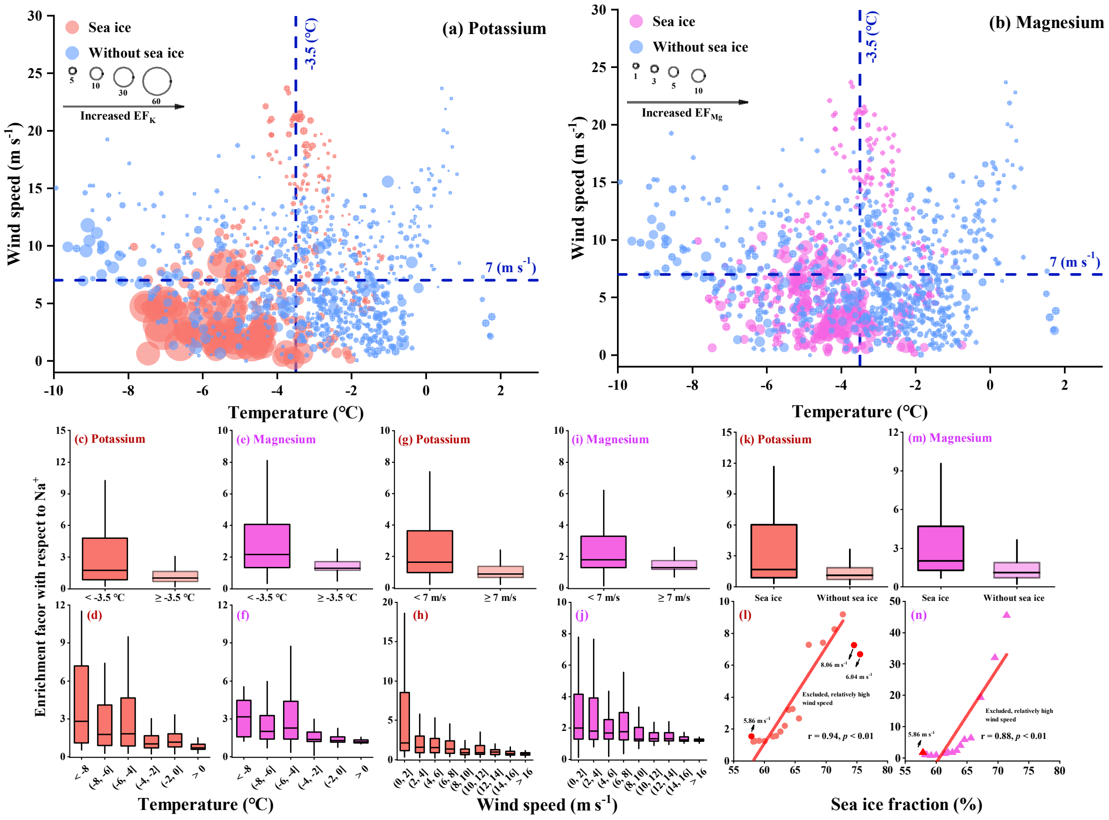

Figure S19

Bubble charts of hourly (a) K^+ and (b) Mg^{2+} enrichment factors with respect to Na^+ at the ambient temperatures, wind speeds, and sea ice fraction. The enrichment factors of K^+ and Mg^{2+} with respect to Na^+ varied as a function of the ambient temperature (c-f), wind speed (g-j), and sea ice fraction (k-n) during the cruise observation. In the box and whisker plot, the lower, median, and upper lines of the box denote the 25th, 50th and 75th percentiles, respectively.

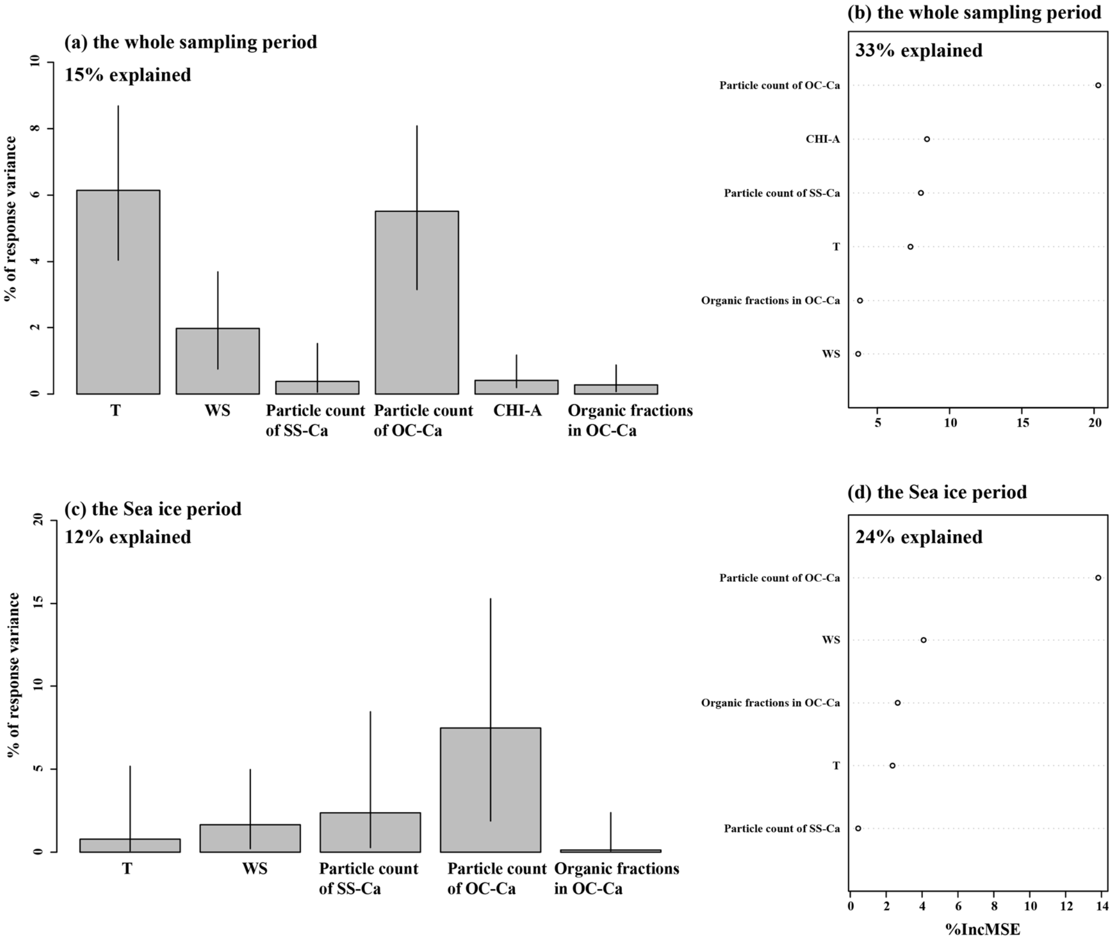

Figure S20

The relative importance of the variation in EF_{Ca}, as determined by multilinear regression for (a) the whole sampling period and (c) the sea ice period. The error bars provide 90% confidence intervals with 100 bootstrap replicates to evaluate the results. The relative importance of the predictors in the random forest analysis for the EF_{Ca} for (b) the whole sampling period and (d) the sea ice period. The %IncMSE, which is used as an indicator for the relative contribution to the predicted variable, refers to the increased mean square error when each independent variable is removed from the predictors.

3. Supplementary Tables

no.	Methodology	EF_{Ca}	EF_{K}	EF_{Mg}	Ref.
1	Laboratory study (fresh and unfiltered seawater)	median = 1.21	n.a.	n.a.	Keene et al. (2007)
2	Field study (Syowa Station, Antarctica)	n.a.	n.a.	1.35-1.55	Hara et al. (2012)
3	Field study (North Atlantic seawater)	~ 100 (45 nm) ~ 10 (80 nm) ~ 4 (150 nm) ~ 2 (200 nm) ~ 1 (500 nm)	~ 5 (45 nm) ~ 1 (80 nm) ~ 1 (150 nm) ~ 1 (200 nm) ~ 1 (500 nm)	~ 2 (45 nm) ~ 1 (80 nm) ~ 1 (150 nm) ~ 1 (200 nm) ~ 1 (500 nm)	Salter et al. (2016)
4	Laboratory study (Artificial seawater)	~ 50 (45 nm) ~ 10 (80 nm) ~ 4 (150 nm) ~ 2.5 (200 nm) ~ 2 (500 nm) ~ 2 (1000 nm)	~ 6 (45 nm) ~ 1 (80 nm) ~ 1 (150 nm) ~ 1 (200 nm) ~ 1 (500 nm) ~ 1 (1000 nm)	~ 2 (45 nm) ~ 1 (80 nm) ~ 1 (150 nm) ~ 1 (200 nm) ~ 1 (500 nm) ~ 1 (1000 nm)	Salter et al. (2016)
5	Laboratory study (Artificial seawater)	~ 5 (56 nm) ~ 1.5 (100 nm) median = 1.14	~ 1.2 (56 nm) ~ 0.3 (100 nm) median = 0.72	~ 1.1 (56 nm) ~ 1 (100 nm) median = 0.83	Cochran et al. (2016)
6	Field study (Arctic Ocean)	geometric mean = 3.7 (from 1.2 to 39)	1 - 8	0.1 - 1	Mukherjee et al. (2020)
7	Field study (the Ross Sea, Southern Ocean)	0.01 - 85, median = 2.76, mean = 1.18	0.20 - 75, median = 3.61, mean = 1.19	0.12 - 26.94, median = 2.46, mean = 1.48	This study

n.a. refers that the value was unavailable.

Note: Enrichment factors of a specific species X with respect to sodium (EF_x) are defined as the ratio of the mass concentration of a specific species X to the mass concentration of sodium in the particle to the same ratio in bulk seawater.

Table S1

A comparative analysis of enrichment factors of a specific species X (EF_X, in which X indicates Ca^{2+}, K^+, and Mg^{2+}) with respect to sodium between previous studies and this study.

Item	leg1 (02.12.2017-20.12.2017)	leg2 (13.01.2018-14.02.2018)	The whole observation
Na (ng m^{-3})	306.72 ± 421.77	395.84 ± 561.04	364.64 ± 561.04
Ca (ng m^{-3})	24.54 ± 41.28	19.38 ± 30.80	21.20 ± 34.96
K (ng m^{-3})	11.39 ± 7.33	8.72 ± 17.65	9.54 ± 15.28
Mg (ng m^{-3})	50.63 ± 48.67	59.61 ± 88.89	56.59 ± 77.47
Cl (ng m^{-3})	18.16 ± 22.18	26.57 ± 36.85	23.63 ± 32.74
EF_{Ca}	3.94 ± 8.50	2.11 ± 4.47	2.76 ± 6.27
Positive calcium enrichment event (%)	71.0%	47.7%	56.0%
EF_{K}	7.93 ± 14.03	1.67 ± 1.69	3.61 ± 8.45
Positive potassium enrichment event (%)	67.9%	54.2%	58.4%
EF_{Mg}	3.74 ± 3.75	1.80 ± 1.05	2.46 ± 2.53
Positive magnesium enrichment event (%)	99.0%	95.2%	96.3%
Temperature (℃)	-4.1 ± 1.4	-3.2 ± 2.2	-3.5 ± 2.0
Wind speed (m s^{-1})	7.2 ± 5.5	7.1 ± 4.2	7.1 ± 4.7
Sea ice fraction	64.91 ± 5.57	54.59 ± 0.08	58.38 ± 6.07
ChI-a concentration (μg L^{-1})	0.51 ± 0.29	0.44 ± 0.18	0.46 ± 0.23
96-Trajectory coverage (%) **Sea ice:** **Open water:** **Antarctic Land:**	92% 4% 4%	30% 12% 58%	52% 9% 39%

Note: During the leg I, the sea ice was retreat. During the leg II, almost no sea ice coverage is equivalent to the sea ice fraction below 55.

Table S2

Average measured ion mass concentrations, enrichment factors for specific cations, and meteorological parameters for leg I and leg II.

Particle types	Major peaks	Particle count		Total particle count
		leg1 (02.12.2017-20.12.2017)	leg2 (13.01.2018-14.02.2018)	
SSA	$[Na]^{+}$, $[Na_2]^{+}$, $[Na^{2}Cl]^{+}$, $[Mg]^{2+}$, [K]+, $[Ca]^{2+}$, and $[Cl]^{-}$	69982	71930	141912
SSA-aged	Inorganic salt signature and nitrate of $[NO_2]$- and $[NO_3]^{-}$	36905	32741	69646
SSA-Bio	Inorganic salt signature and organic matter signals	5489	21276	26765
OC-Ca	$[Ca]^{2+}$ and organic matter signals	134653	284861	419514
OC-K	$[K]^{+}$ and organic matter signals	29734	88549	118283
OC	Organic matter signals	16980	88549	105529
EC	Element carbon with m/z $\pm C_n$, n = 1 - 6	9515	15036	24551

Inorganic salt signatures: $[Na]^{+}$, $[Na_2]^{+}$, $[Na_2Cl]^{+}$, $[Mg]^{2+}$, $[K]^{+}$, $[Ca]^{2+}$, and $[Cl]^{-}$.
Organic matter signals: organic nitrogen ($[CN]^{-}$ and $[CNO]^{-}$), phosphate ($[PO_2]$- and $[PO_3]$-), carbohydrate ($[CHO_2]^{-}$, $[C_2H_3O_2]^{-}$, and $[C_3H_5O_2]^{-}$), siliceous materials ($[SiO_2]^{-}$), and organic carbon ($[C_2H_3]^{+}$ and $[C_2H_3O_3]^{+}$).

Table S3

Particle counts and characteristic peaks for the seven single-particle chemical classes were obtained during cruise observation campaigns.

Item	Area 1 (2018.02.08 22:00-2017.02.10 22:00)	Area 2 (2018.01.22 17:00-2018.01.24 04:00)	Area 3 (2017.12.02 07:00-2017.12.04 19:00)	Area 4 (2017.12.05 00:00-2017.12.05 23:00)	Area 5 (2017.12.18 22:00-2017.12.19 05:00)	leg I	leg II	The whole observation
Duration (h)	**48**	**35**	**61**	**24**	**8**	**426**	**769**	**1195**
EF_{Ca}	10.13 ± 13.63	2.96 ± 2.12	5.47 ± 4.64	9.72 ± 18.75	30.98 ± 31.32	3.94 ± 8.50	2.11 ± 4.47	2.76 ± 6.27
EF_{K}	2.88 ± 2.36	1.49 ± 0.77	n.a.	45.46 ± 14.79	1.22 ± 0.46	7.93 ± 14.03	1.67 ± 1.69	3.61 ± 8.45
EF_{Mg}	2.88 ± 1.54	1.97 ± 0.69	7.89 ± 4.35	8.25 ± 2.90	1.38 ± 0.33	3.74 ± 3.75	1.80 ± 1.05	2.46 ± 2.53
Temperature (℃)	-6.4 ± 1.2	-2.9 ± 0.8	-4.5 ± 0.9	-4.0 ± 0.8	-1.9 ± 2.2	-4.1 ± 1.4	-3.2 ± 2.2	-3.5 ± 2.0
Wind speed ($m\ s^{-1}$)	5.7 ± 3.5	4.7 ± 1.8	6.04 ± 2.2	2.49 ± 1.1	5.1 ± 4.5	7.2 ± 5.5	7.1 ± 4.2	7.1 ± 4.7
Sea ice fraction	54.60 ± 0.02	54.53 ± 0.00	74.28 ± 1.41	71.41	58.06 ± 0.25	64.91 ± 5.57	54.59 ± 0.08	58.38 ± 6.07
Chl-a concentration ($\mu g\ L^{-1}$)	0.99 ± 1.65	0.10± 0.20	Unavailable	Unavailable	Unavailable	0.51 ± 0.29	0.44 ± 0.18	0.46 ± 0.23
96-Trajectory coverage (%)*								
Sea ice:	28%	33%	95%	95%	96%	92%	30%	52%
Open water:	15%	8%	5%	2%	0%	4%	12%	9%
Antarctic Land:	57%	59%	2%	3%	4%	4%	58%	39%

Note: (1) Area 1 and 2 are divided during the leg II, whereas the Area 3, 4, and 5 are divided during the leg I. (2) The values of sea ice fraction and chl-a concentration present with daily resolution. Others present with hourly resolution. (3) No sea ice coverage is equivalent to the sea ice fraction below 55.

Table S4

Average enrichment factors for specific cations and metrological parameters over the different areas mentioned in **Fig. 5** in main text. Although all areas exhibited significant Ca^{2+} enrichment in SSAs, they may have varied due to synergetic environmental factors rather than a single factor. Ca^{2+} enrichment in SSA was notably observed with low wind speed, underscoring the effect of wind speed. The back trajectory coverage is labeled as sea ice, open water, and land.

For leg I, the major positive Ca^{2+} enrichment events were associated with Areas 3, 4, and 5. In addition to the lower wind speed, lower temperature, and the presence of sea ice, the air masses blowing over the large fraction of sea ice and marginal ice zone may play an important role in Ca^{2+} enrichment. For leg II, the major positive Ca^{2+} enrichment events occurred in Areas 1 and 2, which were mainly associated with lower wind speed and temperature. The air masses were mostly from the land-based Antarctic ice.

References

Boreddy, S. K. R. and Kawamura, K.: A 12-year observation of water-soluble ions in TSP aerosols collected at a remote marine location in the western North Pacific: an outflow region of Asian dust, Atmos Chem Phys, 15, 6437-6453, https://doi.org/10.5194/acp-15-6437-2015, 2015.

Cochran, R. E., Jayarathne, T., Stone, E. A., and Grassian, V. H.: Selectivity Across the Interface: A Test of Surface Activity in the Composition of Organic-Enriched Aerosols from Bubble Bursting, J Phys Chem Lett, 7, 1692-1696, https://doi.org/10.1021/acs.jpclett.6b00489, 2016.

Collins, D. B., Zhao, D. F., Ruppel, M. J., Laskina, O., Grandquist, J. R., Modini, R. L., Stokes, M. D., Russell, L. M., Bertram, T. H., Grassian, V. H., Deane, G. B., and Prather, K. A.: Direct aerosol chemical composition measurements to evaluate the physicochemical differences between controlled sea spray aerosol generation schemes, Atmos Meas Tech, 7, 3667-3683, https://doi.org/10.5194/amt-7-3667-2014, 2014.

Gaston, C. J., Furutani, H., Guazzotti, S. A., Coffee, K. R., Bates, T. S., Quinn, P. K., Aluwihare, L. I., Mitchell, B. G., and Prather, K. A.: Unique ocean-derived particles serve as a proxy for changes in ocean chemistry, Journal of Geophysical Research: Atmospheres, 116https://doi.org/10.1029/2010jd015289, 2011.

Gross, D. S., Galli, M. E., Silva, P. J., and Prather, K. A.: Relative sensitivity factors for alkali metal and ammonium cations in single particle aerosol time-of-flight mass spectra, Anal Chem, 72, 416-422, https://doi.org/10.1021/ac990434g, 2000.

Guasco, T. L., Cuadra-Rodriguez, L. A., Pedler, B. E., Ault, A. P., Collins, D. B., Zhao, D. F., Kim, M. J., Ruppel, M. J., Wilson, S. C., Pomeroy, R. S., Grassian, V. H., Azam, F., Bertram, T. H., and Prather, K. A.: Transition Metal Associations with Primary Biological Particles in Sea Spray Aerosol Generated in a Wave Channel, Environ Sci Technol, 48, 1324-1333, https://doi.org/10.1021/es403203d, 2014.

Hara, K., Osada, K., Yabuki, M., and Yamanouchi, T.: Seasonal variation of fractionated sea-salt particles on the Antarctic coast, Geophys Res Lett, 39https://doi.org/10.1029/2012gl052761, 2012.

Healy, R. M., Sciare, J., Poulain, L., Kamili, K., Merkel, M., Muller, T., Wiedensohler, A., Eckhardt, S., Stohl, A., Sarda-Esteve, R., McGillicuddy, E., O'Connor, I. P., Sodeau, J. R., and Wenger, J. C.: Sources and mixing state of size-resolved elemental carbon particles in a European megacity: Paris, Atmos Chem Phys, 12, 1681-1700, https://doi.org/10.5194/acp-12-1681-2012, 2012.

Keene, W. C., Maring, H., Maben, J. R., Kieber, D. J., Pszenny, A. A. P., Dahl, E. E., Izaguirre, M. A., Davis, A. J., Long, M. S., Zhou, X. L., Smoydzin, L., and Sander, R.: Chemical and physical characteristics of nascent aerosols produced by bursting bubbles at a model air-sea interface, Journal of Geophysical Research: Atmospheres, 112https://doi.org/10.1029/2007jd008464, 2007.

Lundberg, S. M., Erion, G., Chen, H., DeGrave, A., Prutkin, J. M., Nair, B., Katz, R., Himmelfarb, J., Bansal, N., and Lee, S. I.: From local explanations to global understanding with explainable AI for trees, Nat Mach Intell, 2, 56-67, https://doi.org/10.1038/s42256-019-0138-9, 2020.

Mukherjee, P., Reinfelder, J. R., and Gao, Y.: Enrichment of calcium in sea spray aerosol in the Arctic summer atmosphere, Mar Chem, 227https://doi.org/10.1016/j.marchem.2020.103898, 2020.

Prather, K. A., Bertram, T. H., Grassian, V. H., Deane, G. B., Stokes, M. D., DeMott, P. J., Aluwihare, L. I., Palenik, B. P., Azam, F., Seinfeld, J. H., Moffet, R. C., Molina, M. J., Cappa, C. D., Geiger, F. M., Roberts, G. C., Russell, L. M., Ault, A. P., Baltrusaitis, J., Collins, D. B., Corrigan, C. E., Cuadra-Rodriguez, L. A., Ebben, C. J., Forestieri, S. D., Guasco, T. L., Hersey, S. P., Kim, M. J., Lambert,

W. F., Modini, R. L., Mui, W., Pedler, B. E., Ruppel, M. J., Ryder, O. S., Schoepp, N. G., Sullivan, R. C., and Zhao, D. F.: Bringing the ocean into the laboratory to probe the chemical complexity of sea spray aerosol, P Natl Acad Sci USA, 110, 7550-7555, https://doi.org/10.1073/pnas.1300262110, 2013.

Pratt, K. A. and Prather, K. A.: Mass spectrometry of atmospheric aerosolsuRecent developments and applications. Part II: On-line mass spectrometry techniques, Mass Spectrom Rev, 31, 17-48, https://doi.org/10.1002/mas.20330, 2012.

Qin, X. Y., Bhave, P. V., and Prather, K. A.: Comparison of two methods for obtaining quantitative mass concentrations from aerosol time-of-flight mass spectrometry measurements, Anal Chem, 78, 6169-6178, https://doi.org/10.1021/ac060395q, 2006.

Salter, M. E., Hamacher-Barth, E., Leck, C., Werner, J., Johnson, C. M., Riipinen, I., Nilsson, E. D., and Zieger, P.: Calcium enrichment in sea spray aerosol particles, Geophys Res Lett, 43, 8277-8285, https://doi.org/10.1002/2016gl070275, 2016.

Schlitzer, R.: Interactive analysis and visualization of geoscience data with Ocean Data View, Comput Geosci-Uk, 28, 1211-1218, https://doi.org/10.1016/S0098-3004(02)00040-7, 2002.

Sierau, B., Chang, R. Y. W., Leck, C., Paatero, J., and Lohmann, U.: Single-particle characterization of the high-Arctic summertime aerosol, Atmos Chem Phys, 14, 7409-7430, https://doi.org/10.5194/acp-14-7409-2014, 2014.

Song, C., Becagli, S., Beddows, D. C. S., Brean, J., Browse, J., Dai, Q., Dall'Osto, M., Ferracci, V., Harrison, R. M., Harris, N., Li, W., Jones, A. E., Kirchgäßner, A., Kramawijaya, A. G., Kurganskiy, A., Lupi, A., Mazzola, M., Severi, M., Traversi, R., and Shi, Z.: Understanding Sources and Drivers of Size-Resolved Aerosol in the High Arctic Islands of Svalbard Using a Receptor Model Coupled with Machine Learning, Environ Sci Technol, 56, 11189-11198, https://doi.org/10.1021/acs.est.1c07796, 2022.

Su, B., Wang, T., Zhang, G., Liang, Y., Lv, C., Hu, Y., Li, L., Zhou, Z., Wang, X., and Bi, X.: A review of atmospheric aging of sea spray aerosols: Potential factors affecting chloride depletion, Atmos Environ, 290https://doi.org/10.1016/j.atmosenv.2022.119365, 2022.

Su, B. J., Zhang, G. H., Zhuo, Z. M., Xie, Q. H., Du, X. B., Fu, Y. Z., Wu, S., Huang, F. G., Bi, X. H., Li, X., Li, L., and Zhou, Z.: Different characteristics of individual particles from light-duty diesel vehicle at the launching and idling state by AAC-SPAMS, Journal of Hazardous Materials, 418https://doi.org/10.1016/j.jhazmat.2021.126304, 2021a.

Su, B. J., Zhuo, Z. M., Fu, Y. Z., Sun, W., Chen, Y., Du, X. B., Yang, Y. X., Wu, S., Xie, Q. H., Huang, F. G., Chen, D. H., Li, L., Zhang, G. H., Bi, X. H., and Zhou, Z.: Individual particle investigation on the chloride depletion of inland transported sea spray aerosols during East Asian summer monsoon, Sci Total Environ, 765https://doi.org/10.1016/j.scitotenv.2020.144290, 2021b.

Yan, J., Jung, J., Lin, Q., Zhang, M., Xu, S., and Zhao, S.: Effect of sea ice retreat on marine aerosol emissions in the Southern Ocean, Antarctica, Sci Total Environ, 745, 140773, https://doi.org/10.1016/j.scitotenv.2020.140773, 2020a.

Yan, J., Jung, J., Zhang, M., Xu, S., Lin, Q., Zhao, S., and Chen, L.: Significant Underestimation of Gaseous Methanesulfonic Acid (MSA) over Southern Ocean, Environ Sci Technol, 53, 13064-13070, https://doi.org/10.1021/acs.est.9b05362, 2019.

Yan, J., Jung, J., Zhang, M., Bianchi, F., Tham, Y., Xu, S., Lin, Q., Zhao, S., Li, L., and Chen, L.: Uptake selectivity of methanesulfonic acid (MSA) on fine particles over polynya regions of the Ross Sea, Antarctica, Atmos Chem Phys, 20, 3259-3271, https://doi.org/10.5194/acp-20-3259-2020, 2020b.

Zhang, G., Fu, Y., Peng, X., Sun, W., Shi, Z., Song, W., Hu, W., Chen, D., Lian, X., Li, L., Tang, M., Wang, X., and Bi, X.: Black Carbon Involved Photochemistry Enhances the Formation of Sulfate in the Ambient Atmosphere: Evidence From In Situ Individual Particle Investigation, Journal of Geophysical Research: Atmospheres, 126https://doi.org/10.1029/2021jd035226, 2021.